Digital Discovery

ROYAL SOCIETY OF CHEMISTRY

PAPER

Published on 03 August 2026

Cite this: DOI: 10.1039/d6dd00149a

Unlocking a shortcut: acceleration of non-aqueous electrolyte development by active machine learning for sodium-based batteries

Mirko Fischer, †[a] Robert Tobias Hinz, †[b] Christian Wölke, [b] Isidora Cekic-Laskovic, [b] Martin Winter [bc] and Andreas Heuer *[a]

Sodium-based batteries are promising candidates for sustainable large-scale energy storage, yet systematic electrolyte design remains challenging due to the high dimensionality and physical constraints of formulation space. Here, we present a data-driven workflow that combines high-throughput experimentation with batch-wise active learning to efficiently map and model non-aqueous sodium-based electrolyte formulations. Rather than targeting a single optimal composition, the approach constructs predictive surrogate models over the full space of physically admissible formulations, which in the present case corresponds to a three-dimensional, compositionally constrained feature space defined by salt content and solvent mixing ratios. Training identical models on sodium- and lithium-based data sets enables a direct, composition-wide comparison of both cations within the same solvent framework, revealing largely similar conductivity landscapes with modest but systematic differences that can be rationalized by differences in ionic size and solvation characteristics. The formulation space can be reliably described using only 72 electrolyte compositions acquired in two active learning iterations, corresponding to a reduction in required experiments by a target-dependent factor, which is 4–7 for the ionic conductivity at 40 °C, compared to random sampling. Conductivity-guided electrolyte selection leads to improved rate capability and low-temperature performance in sodium-ion full cells, while also highlighting the limitations of ionic conductivity as a sole performance descriptor. Overall, this work establishes a transferable, physics-informed framework for data-efficient electrolyte exploration.

Received 26th March 2026
Accepted 19th July 2026

DOI: 10.1039/d6dd00149a

rsc.li/digitaldiscovery

1 Introduction

The transition to a renewable energy economy relies heavily on the development of efficient and sustainable energy storage solutions. Overcoming rising challenges by advancing battery technologies that prioritize longevity, sustainability, safety, and affordability is therefore of critical importance. Sodium-based batteries (SBBs), which offer a promising alternative to traditional Li-based counterparts, show potential advantages in terms of cost, availability of raw materials, and reduced environmental impact. Despite their potential, however, SBBs face substantial technical barriers that must be addressed through continued research and development. By overcoming these challenges, sodium-based batteries can fulfill their promise as a game-changing technology for large-scale energy storage, enabling a more rapid and widespread adoption of renewable energy sources.[1–3] Electrolytes play a crucial role in determining the performance and stability of SBBs, as they enable the transport of Na^+ ions, facilitate the formation of the solid electrolyte interphase (SEI), and influence the reversibility of sodium intercalation and metal deposition. These factors have a profound impact on the galvanostatic cycling stability, efficiency, and safety of SBBs. However, the development of suitable electrolytes for SBBs is complicated by several key factors, including the increased reactivity of sodium metal, the lower Lewis acidity of sodium ions, and the differing solubility and ionic conductivity of sodium salts in electrolytes.[4–9] One of the core electrolyte properties worth considering in this context is the ionic conductivity, as higher ionic conductivity is generally associated with reduced internal cell resistance and improved rate capability.[8] At the same time, a direct and universal correlation between ionic conductivity and overall cell performance has not been established, particularly for the less explored case of Na-based non-aqueous electrolytes, and must therefore be examined with care when formulating electrolytes aimed at enhancing the performance and stability of SBBs.

To overcome traditional trial-and-error approaches based on manual and largely serial variation of electrolyte compositions,

[a]Institute of Physical Chemistry, University of Münster, Corrensstraße 28/30, 48149 Münster, Germany. E-mail: andreas.heuer@uni-muenster.de

[b]Helmholtz-Institute Münster (IMD-4), Forschungszentrum Jülich GmbH, Corrensstraße 48, 48149 Münster, Germany

[c]MEET Battery Research Center, University of Münster, Corrensstraße 46, 48149 Münster, Germany

† These authors contributed equally to this work.

researchers are increasingly employing high-throughput experimentation (HTE) methods. These approaches enable the simultaneous execution of numerous experiments under precise and well-controlled conditions. In combination with advanced and tailored data analysis methods, HTE accelerates discovery by systematically exploring large compositional parameter spaces and efficiently identifying promising electrolyte formulations. While HTE is a well-established tool in pharmaceuticals,[10,11] catalysis,[12–14] and materials science,[15,16] its adoption in battery research has progressed more slowly. This is mainly due to the electrochemical complexity of electrolytes, the strong coupling of multiple components, the high costs and technical demands of automation, and the challenges associated with handling and interpreting large data sets. Nonetheless, as the demand for safer, sustainable, and higher-performance energy storage systems intensifies, the integration of HTE with machine learning and robotic experimentation—demonstrated in recent platforms for electrolyte and electrode optimization—holds tremendous promise to expedite the design and refinement of SBBs and next-generation energy systems.[17–23]

The efficiency of coupling robotic HTE with machine learning has been demonstrated for a wide range of systems, including aqueous, non-aqueous, and polymer electrolytes based on lithium- and sodium-conducting salts. Dave *et al.*[24] developed a robotic platform named "Clio", which automatically formulates electrolytes from feeder solutions and subsequently determines their density, viscosity, and ionic conductivity. In combination with a Bayesian Optimizer (BO), this platform enabled closed-loop, iterative optimization of electrolyte compositions for lithium hexafluorophosphate ($LiPF_6$) dissolved in mixtures of ethylene carbonate (EC), ethyl methyl carbonate (EMC), and dimethyl carbonate (DMC), with the primary goal of efficiently identifying locally optimal formulations. Zhu *et al.*[25] further advanced this approach by replacing BO with geometric deep learning, demonstrating improved extrapolative performance for predictions at previously unseen temperatures. Another robotic platform, "Otto", successfully optimized aqueous sodium electrolytes by formulating and analyzing 140 compositions within only 40 h, again relying on BO-driven iterative optimization.[26] Various related approaches have been developed to improve the prediction of ionic conductivity using BO-based or one-shot active learning (AL) strategies, including grid-based data sets and robotic platforms for polymer electrolyte processing.[27,28] Beyond ionic conductivity optimization, similar closed-loop platforms have also been applied to predict and enhance the solubility of redox-active organic molecules for redox flow batteries or to maintain high discharge capacity in aqueous electrolytes.[29,30]

In this paper, we establish a high-throughput, data-driven workflow to map and model non-aqueous Na-based electrolyte formulations using batch-wise active learning and the Liquid Electrolyte Composition Analysis (LECA) package introduced in our previous work (Fig. 1a).[22] In that work, based on a hand-crafted data set we performed a data-driven analysis of the composition-dependent ionic conductivity of non-aqueous lithium-based electrolytes to investigate the interplay between different components and identify temperature-dependent optimal electrolyte formulations. In contrast to closed-loop studies that primarily aim at identifying a single optimal composition *via* Bayesian optimization, the central objective in this work is to construct a predictive, physically meaningful surrogate model that covers the full space of feasible electrolyte formulations, including sub-optimal regions, and thereby quantifies the influence of individual components on ionic conductivity across temperature (Fig. 1b). To this end, a new Na-based electrolyte data set is generated in a manner compatible with parallel HTE, enabling high model fidelity with a minimal number of experiments and active-learning iterations. Electrolyte compositions based on $NaPF_6$ in mixtures of ethylene carbonate (EC), propylene carbonate (PC), and ethyl methyl carbonate (EMC) are investigated between −20 °C and 60 °C as a well-defined proof-of-concept system (Fig. 2). Owing to the holistic coverage of composition space, the resulting surrogate models enable a direct, composition-wide comparison between Na- and Li-based electrolytes within an identical feature representation. For this purpose, the Na-based data are compared to a corresponding Li-based reference data set from our previous work, allowing similarities and differences in ionic conductivity to be assessed across the entire phase space rather than at isolated compositions (Fig. 1c).[22] Beyond the experimental data set, numerical active-learning simulations are employed to analyze how model accuracy scales with data set size and to quantify the efficiency gains of active learning compared to random sampling in low-dimensional, physically constrained chemical spaces. While optimization is not the primary goal of this study, the trained surrogate models enable the identification of temperature-specific high-conductivity formulations (Fig. 1c). These model-selected electrolytes are evaluated as targeted test cases in layered oxide‖hard carbon sodium-ion coin cells and benchmarked against established reference formulations using rate capability and cycling tests to probe how conductivity-driven electrolyte selection manifests at the lab-cell level.

2 Technical and model aspects

2.1 Data preparation

Before training the ML models on the ionic conductivity, the data were preprocessed following an extended pipeline introduced and discussed in detail in our previous publications.[22,31] Here, the main steps are briefly summarized, and additional preprocessing steps introduced for the Na-based data set are described, aiming to improve robustness and automation for future autonomous-laboratory applications.

The raw data consist of the electrolyte composition (in mmol and g) and the measured ionic conductivities (in S cm^{-1}). Overall, 1944 individual measurements were available in the Na-based data set.

An automated outlier detection based on HDBSCAN[32] was used to identify measurements affected by experimental artifacts prior to further data processing, including unphysical negative ionic conductivity values. Furthermore, an additional filtering criterion was applied as follows: for the Na-based

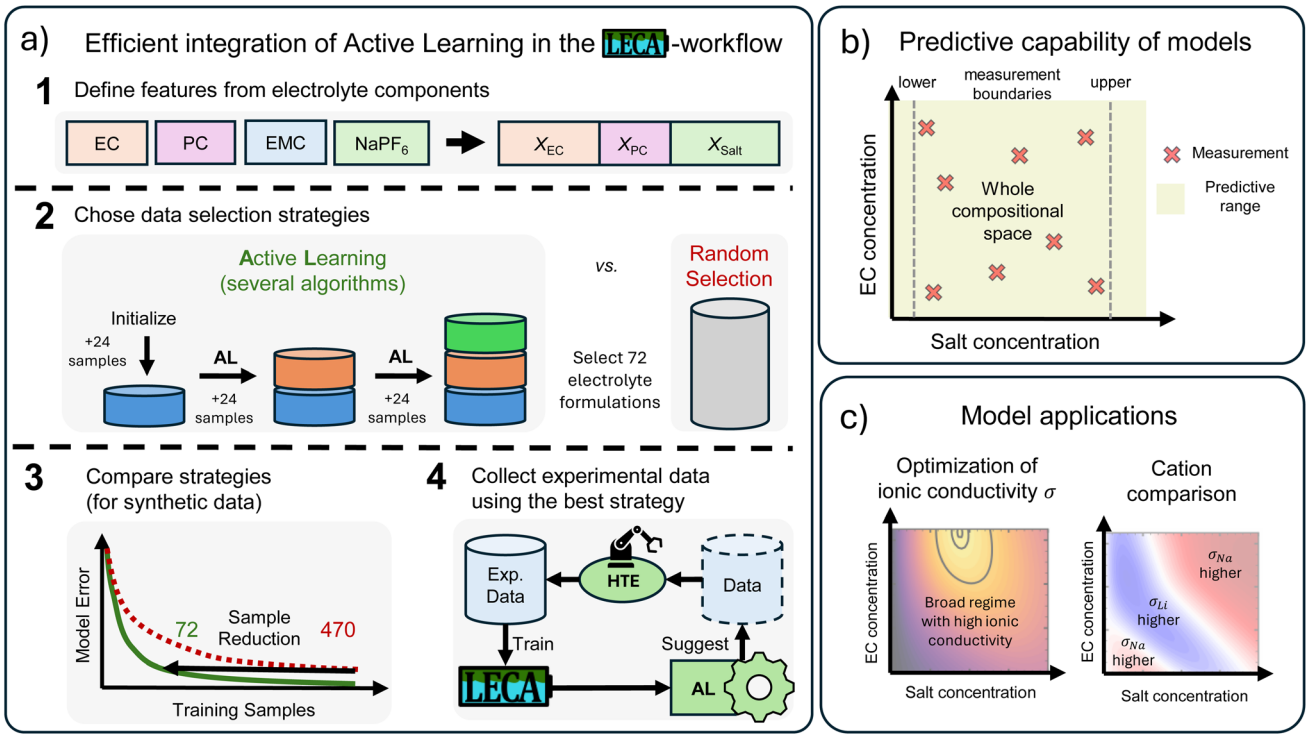

Fig. 1 (a) Integration of active learning in the LECA-workflow. First, features were defined, followed by the identification and implementation of suitable acquisition functions. All acquisition functions were compared before collecting any experimental data. Fitted models (b) enabled reliable predictions for the full feature space, even extending the experimental boundary conditions for the salt concentration and (c) were applied to identify electrolyte formulations with maximum ionic conductivity and to compare sodium and lithium as cations in otherwise similar electrolyte formulations.

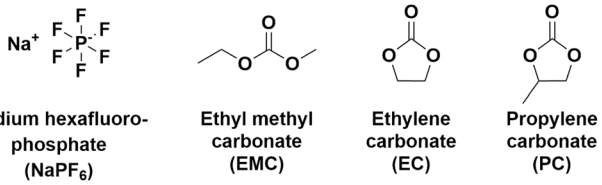

Fig. 2 Chemical structures of the conducting salt and solvents used for the electrolyte preparation.

electrolytes, the ionic conductivity was measured three times for each composition and temperature to minimize experimental effort. If one measurement deviated substantially from the other two ($\Delta\log(\sigma) > 0.1$), it was classified as an outlier and removed.

Whereas HDBSCAN detected no extreme outliers, indicating generally consistent measurements, 50 measurements were removed first due to negative ionic conductivity (*i.e.* measurement artifacts) and afterwards 92 due to deviations of one of three measurements at a specific temperature.

To obtain a low-dimensional and physically meaningful feature representation that allows continuous exploration of composition space, generalized molar solvent features (mol mol^{-1}) were defined as

$$x_{\text{solvent } j} = \frac{N(\text{solvent } j)}{\sum_{i=j}^{n_{\text{solvent}}} N(\text{solvent } i)}, \quad (1)$$

with $j \in (1, 2, \ldots, n)$. The solvent-related features were calculated using the ordering $j \in$ (PC, EC, EMC). This definition can be generalized to an arbitrary number of solvents and thus extends the applicability of the present approach. The feature $x_{\text{solvent } n}$ is always unity within this definition and can therefore be omitted.

The feature corresponding to the total conducting salt concentration was defined as

$$x_{\text{salt}} = \frac{\sum_{k=1}^{n_{\text{salt}}} (\text{salt } k)}{\sum_{k=1}^{n_{\text{salt}}} N(\text{salt } k) + \sum_{i=1}^{n_{\text{solvent}}} N(\text{solvent } i)}. \quad (2)$$

Since only $NaPF_6$ was used as a conducting salt for the Na-based electrolytes, no additional salt-related features were required. This choice is motivated by the linear dependence observed when utilizing two conducting salts.[22] In cases with two or more conducting salts, an analogous scheme to that used for the solvents can be applied to define salt-related features.

In total, the Na-based electrolytes are fully described by only three features: x_{Salt}, x_{PC}, and x_{EC}. All features take values in the

interval (0, 1), ensuring that every combination of feature values corresponds to a physically meaningful electrolyte composition.

To obtain a well-behaved regression target in the dilute-salt limit, we modelled the salt-normalized ionic conductivity $\log(\sigma/x_{\mathrm{Salt}})$ instead of σ directly. The logarithmic transformation accounts for the wide dynamic range of σ, while normalization by x_{Salt} ensures a finite target as $x_{\mathrm{Salt}} \to 0$ under physically expected low-concentration scaling. This choice stabilizes model behavior near the boundaries of composition space and prevents nonphysical predictions of negative ionic conductivity.

To account for the temperature dependence of the ionic conductivity, an Arrhenius-type fit was applied,

$$\begin{aligned}\log\left(\frac{\sigma}{x_{\mathrm{Salt}}}\right) &= S_0^*(X) - \log x_{\mathrm{Salt}} - S_1(X)(\beta-\beta_0) - S_2(X)(\beta-\beta_0)^2 \\ &= S_0(X) - S_1(X)(\beta-\beta_0) - S_2(X)(\beta-\beta_0)^2,\end{aligned} \tag{3}$$

thereby transforming the objective $\log(\sigma/x_{\mathrm{Salt}})$ into three separate targets: S_0, corresponding to the ionic conductivity at the onset temperature T_0; S_1, corresponding to an onset-temperature-dependent activation energy; and S_2, describing deviations from Arrhenius behavior.[22,33,34] The onset temperature T_0 was chosen such that S_0 and S_1 are largely uncorrelated, yielding robust and interpretable targets. Note that the choice of the onset temperature has no significant effect on the Arrhenius fit and the mean model prediction. However, uncertainties are larger when increasing the difference between onset temperature and predictive temperature (see also SI subsection S4.1). For the Na-based data set, $T_0 = 40$ °C was selected.

This transformation serves four purposes: it provides additional physical insight through the separate targets, eliminates temperature as an explicit feature, and substantially reduces the number of data points by associating one data point with each electrolyte formulation rather than with each temperature. Thereby it also increases statistical stability since measurements at other temperatures are also taken into account to determine the ionic conductivity at a specific temperature.

To estimate statistical uncertainties of the Arrhenius-fit parameters, we applied bootstrapping by fitting each electrolyte using repeated resamples of the available measurements.[35] The resulting spread of fitted parameters provides uncertainty estimates for each S_i, reflecting finite-sample variability (including measurement scatter and potential model misfit).

Following an initial Arrhenius fit, data points deviating significantly from the fitted behavior ($\Delta\log(\sigma) > 0.15$) were identified, flagged as outliers, and removed. A second Arrhenius fit was then performed on the cleaned data set and used for subsequent model training and analysis. Note that in most cases only data points at a single temperature were removed, however for 3 electrolyte formulations, data was systematically removed below $T = 10$ °C. In one case the measured ionic conductivity was significantly below the prediction of the Arrhenius fit. This indicated a phase transition, which could be explained by known crystallization of electrolytes with high EC concentration (see SI subsection S4.1 for further information). Whereas removing those data increases the accuracy of the Arrhenius description at higher temperatures, the description at low temperatures may be inaccurate if significant non-Arrhenius behavior occurs.

Using this filtering procedure, 16 data points were removed additionally to the 142 data points removed during previous steps. The remaining 1786 data points were then used for the second Arrhenius fit.

The Li-based electrolyte data set used for the direct comparison of Na and Li cations was prepared in accordance with this scheme, with two differences relative to the Na-based data. First, each electrolyte was measured at least five times per temperature. Second, owing to the larger number of measurements, only a single Arrhenius fit was performed and directly used for model training. The onset temperature was set to $T_0 = 60$ °C.

2.2 Model training

In this study, a small feed-forward neural network (NN)[36,37] was employed within the LECA package and implemented in scikit-learn.[38] The network consists of two hidden layers with 16 neurons per layer. This deliberately compact architecture reflects the low-dimensional and physically constrained feature space and enables accurate regression without the need for deep or highly expressive models, thereby reducing the risk of overfitting. As activation function, the hyperbolic tangent was used, and the LBFGS optimizer[39] was employed with a constant learning rate of 0.001 and L2 regularization ($\lambda = 0.008$). The selection of this model was made previous to any data collection and validated afterwards by comparing the performance of different hyperparameters and model types (see Section S6).

While AL was performed exclusively using the NN model, an additional Gaussian process regression (GPR) model[40,41] with an anisotropic Matérn kernel was trained on the final data set to compare predictions obtained from different model classes. This choice was motivated by previous results, where the NN achieved the highest predictive accuracy, followed by the GPR model, for Li-based electrolyte conductivity prediction.[22]

For models trained on the complete data set after completion of the AL procedure, both five-fold and leave-one-out (LOO) cross-validation were used to assess predictive performance.

In contrast to previous studies, the present work does not aim at directly optimizing a single electrolyte composition. Instead, the focus is on reducing prediction errors across the full feature space, explicitly including sub-optimal formulations. This strategy enables a reliable and comprehensive characterization of the entire space of feasible electrolyte compositions rather than only its optimum. In addition, by employing a batch-wise AL strategy, the need for iterative, serial sampling is avoided, allowing the full potential of parallel HTE to be exploited.

2.3 Acquisition functions

To reduce experimental time and cost, traditional trial-and-error-based experimental planning can be replaced by data-driven strategies. This is particularly important for high-dimensional search spaces, where individual features may

have a strongly varying influence on the target property (see SI Section S5).

AL algorithms dynamically adapt both feature relevance and data distribution during model construction.[42–45] To establish a comprehensive data set for Na-based electrolytes, an AL strategy which relies on acquisition functions was adopted. It starts from a small number of initially selected data points and iteratively proposes additional batches of experiments. As the AL process evolves, the existing model is continuously evaluated and expanded by selecting new data points that most effectively improve predictive performance. This enables a systematic and efficient exploration of the relevant composition space while minimizing experimental effort.

For effective integration into a HTE framework, several requirements for the acquisition function were identified:

The acquisition function should (1) propose new data points in continuous feature space (population-based AL) rather than being restricted to a predefined pool (pool-based AL). (2) Support batch-wise proposal of new data points to enable parallel experimentation, as serial single-point acquisition is inefficient in an HTE context. (3) Balance informativeness and diversity.[46–48] New data points should both reduce model uncertainty and increase coverage of feature space to limit extrapolation and overfitting. (4) Optimize model accuracy across the full feature space (surrogate based-modelling) rather than only near an optimum (surrogate-based optimization), as typically pursued in classical BO with acquisition functions like probability of improvement (PI) or expected improvement (EI). However, there are strong synergies between certain AL algorithms, which make use of acquisition functions, and classical BO, which uses acquisition functions, too. Whereas in AL the acquisition functions serve the goal to minimize the model error, in BO a quick identification of the optimum of a function should be achieved. Both approaches can be seen therefore as a member of the family of acquisition function-based goal-driven learning approaches.[49,50] (5) Be applicable to different model architectures, including Gaussian process regression (GPR), linear regression (LR),[36] random forest (RF),[51] and neural networks (NN).

Based on these criteria, three greedy acquisition functions[52] were implemented: GSx, GSy, and iGS, which maximize distances between data points in feature space, objective space, or both, respectively.[53,54] In addition, the negative integrated posterior variance (NIPV) as an example of a Bayesian Active Learning acquisition function[55,56] and the inverse-distance-based exploration for active learning (IDEAL) acquisition function[46] were employed. Details of the individual acquisition functions are provided in the original publications and in the SI (Section S1).

GSx, GSy, and iGS natively satisfy requirements (1), (4), and (5), while IDEAL additionally fulfills requirement (3). NIVP also satisfies requirement (1), (3) and (4) but not (5), since it requires Bayesian models like GPR. All acquisition functions generate data points sequentially. Requirement (2) was realized by iteratively augmenting the training set with predicted values for newly proposed points, allowing additional candidates to be generated and combined into batches. After experimental evaluation, the predicted values were replaced by the corresponding measurements. This procedure was repeated until predefined accuracy criteria were met.

2.4 Implementation of an active learning loop into experiments

To construct a predictive model within a closed experimental–computational loop, data acquisition was organized into successive generations (Gen), with AL-based model updates performed in between. Based on initial benchmarking, the IDEAL acquisition function was selected for all subsequent iterations, using a balancing parameter $\lambda = 10$, which provided an effective trade-off between informativeness and diversity (see SI Section S7).[46]

The initial batch of data points was generated using the model-free GSx approach.[54] Subsequent batches were proposed using IDEAL. The feature x_{Salt} was limited to be selected within the interval (0.05, 0.20), which corresponds roughly to salt concentrations between 0.5 and 2.7 mol kg^{-1} and ensures reasonable electrolyte formulations. The features x_{EC} and x_{PC} were selected from the interval (0.0, 1.0). The first batch is referred to as Gen0, followed by Gen1 and Gen2. Each generation comprised 24 distinct electrolyte compositions with three replicate samples each, corresponding to 72 parallel experiments per generation. It was verified that moderate variations in batch size do not substantially affect the outcome of the AL procedure (see SI Section S7).

As the objective function for the acquisition function, the ionic conductivity at $T = 20$ °C was chosen. This quantity was obtained from predictions of the Arrhenius parameters S_i using eqn (3). As a consequence of this choice, S_0 carries a higher weight than S_1 and S_2 near the onset temperature T_0, while the influence of S_1 and S_2 increases at significantly lower or higher temperatures. Guided by our previous work,[22] prioritizing S_0 was therefore a natural choice, as its comparatively high experimental accuracy allows it to benefit most strongly from increased data availability.

3 Results

3.1 Model predictions for Na-based electrolytes and comparison to Li-based electrolytes

When comparing all features, x_{Salt} and x_{EC} exhibit a considerably higher influence on the ionic conductivity than x_{PC}, in particular for high-temperature applications, where the predicted contribution of x_{PC} vanishes in electrolyte formulations with high ionic conductivity. The following analysis therefore focuses on these two dominant features. When comparing different model types, the NN and GPR models showed very similar prediction errors in leave-one-out cross-validation (see SI Section S8). While the GPR model performed slightly better in predicting S_0 and S_1, the NN model showed a small advantage for S_2. In the following, results obtained from the NN model are discussed.

Since the newly generated Na-based electrolyte data set and the previously established Li-based data set differ only in the

employed Na^+ and Li^+ cations, their influence on ionic conductivity can be compared directly. For the Li-based electrolytes, $x_{LiPF_6} = 1$ was set, such that PF_6^- was treated as the common salt anion. Fig. 3 illustrates NN-based predictions of the ionic conductivity at $T = 20$ °C for Na- and Li-based electrolytes as functions of x_{Salt} and x_{EC}, while keeping $x_{PC} = 0$ constant. The corresponding difference between Na- and Li-based predictions is also shown, highlighting regions in which either lithium or sodium exhibits higher ionic conductivity. In Fig. 3a–c, $\log(\sigma/x_{Salt})$ is shown as a function of x_{EC} and x_{Salt} on a logarithmic scale. Additionally, Fig. 3d and e display the ionic conductivity σ on a linear scale.

When comparing sodium to lithium, the largest differences in ionic conductivity are observed at low conducting salt and EC concentrations. In this regime, the ionic conductivity of the Li-based electrolyte depends strongly on the EC concentration, whereas the EC concentration plays a less crucial role in the Na-based electrolyte. As a result, the Na-based electrolyte exhibits a higher ionic conductivity in this low-salt, low-EC regime. Note that no training data are available for very low conducting salt concentrations below $x_{Salt,Na} < 0.05$ for Na-based and $x_{Salt,Li} < 0.015$ for Li-based electrolytes, such that the models extrapolate in this region. However, it was verified that the associated model uncertainties are substantially smaller than the observed differences between the Na- and Li-based predictions in this regime (see SI Section S9).

Second, the maximum ionic conductivity is only slightly higher for the Na-based electrolyte ($\sigma_{Na}^{max} = 9.2$ mS cm^{-1}) than for the Li-based electrolyte ($\sigma_{Li}^{max} = 8.6$ mS cm^{-1}), while both systems exhibit comparable maximum conductivities in the optimal composition regime. Furthermore, exchanging Li by Na leads to a shift of the conductivity maximum toward higher conducting salt concentrations ($x_{Salt,Li}^{max} = 0.065$ to $x_{Salt,Na}^{max} = 0.086$) and higher EC concentrations ($x_{EC,Li}^{max} = 0.56$ to $x_{EC,Na}^{max} = 0.64$). Notably, no sharp optimum is observed. Instead, a broad region of high ionic conductivity is present for both electrolytes, as indicated by the 99.9%, 99% and 90% contour levels. The extent of these high-conductivity regions is comparable for the Li- and Na-based electrolytes.

For $x_{Salt} = 0.086$, corresponding approximately to a conducting salt concentration of 1 mol kg^{-1}, a pronounced dependence of the salt-normalized ionic conductivity on the EC concentration is observed for both electrolyte systems. In both cases, $\log(\sigma/x_{Salt})$ increases from approximately −1.54 at zero EC

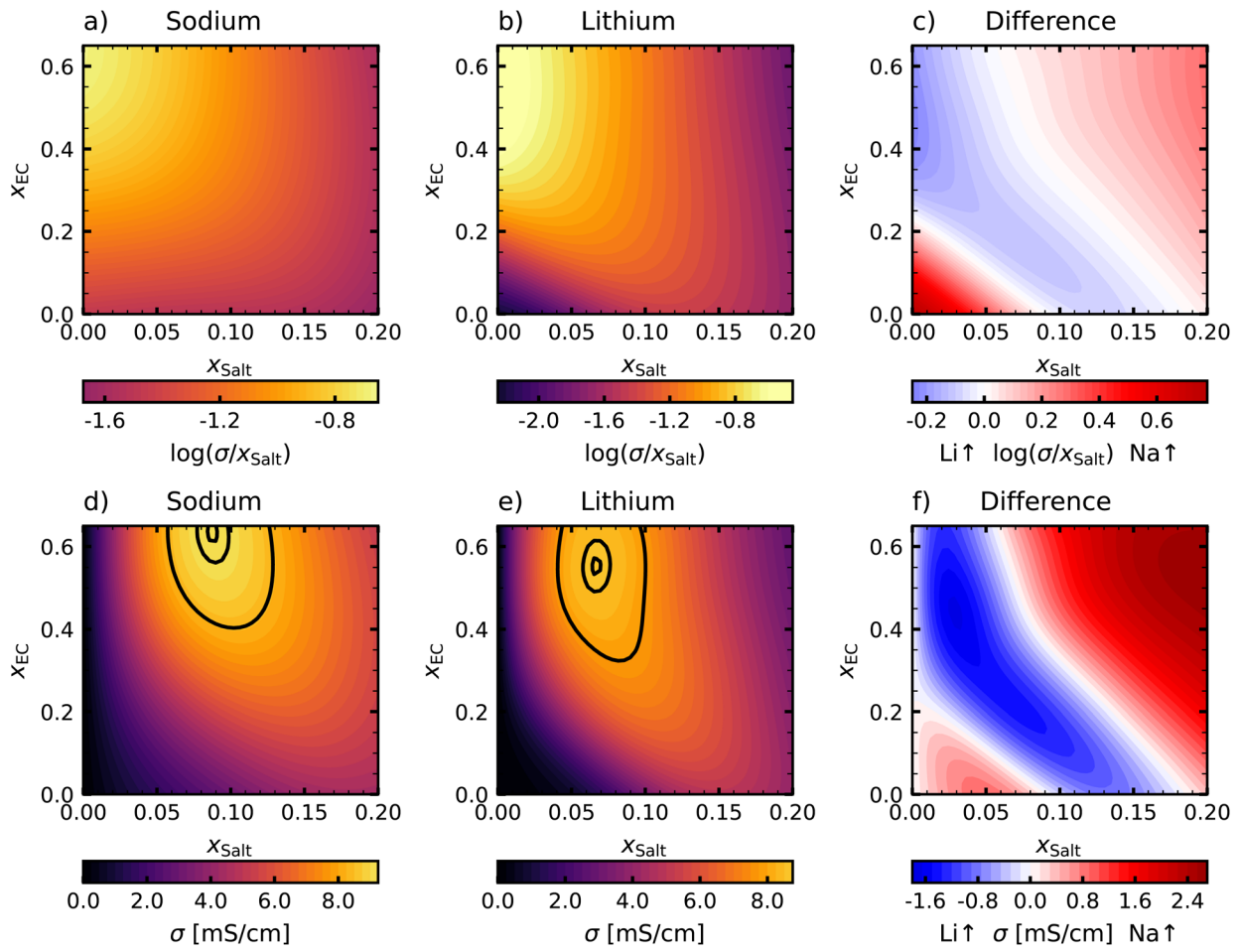

Fig. 3 (a) and (b) Predictions of $\log(\sigma/x_{Salt})$ for Li- and Na-electrolytes dependent on x_{Salt} and x_{EC} and (c) difference of $\log(\sigma/x_{Salt})$ between Li and Na. (d) and (e) Predictions of σ for Li- and Na-electrolytes and (f) difference of σ between Li and Na.

content to about −1.02 for the Li-based electrolyte and −0.97 for the Na-based electrolyte before entering a plateau regime. The plateau in $\log(\sigma/x_{\mathrm{Salt}})$ is reached at relatively high EC fractions of $x_{\mathrm{EC}} \approx 0.5$ for the Na-based electrolyte and at a lower EC fraction of $x_{\mathrm{EC}} \approx 0.4$ for the Li-based electrolyte. While the salt-normalized ionic conductivity increases nearly monotonically over the full EC range in the Na-based system, the increase in the Li-based electrolyte is largely confined to EC fractions below $x_{\mathrm{EC}} \approx 0.2$ (see also SI Section S9 for further details).

This behavior is consistent with previous studies combining simulations and experiments.[57] The influence of EC concentration can be rationalized by its higher dielectric constant compared to EMC, which facilitates the weakening of cation–anion associations and thereby reduces correlated ion motion, leading to an increase in ionic conductivity. In general, owing to its higher Lewis acidity, Li interacts more strongly with EC than Na.[58]

At higher conducting salt concentrations, the influence of EC concentration on ionic conductivity decreases and becomes negligible for the Li-based electrolytes. This can be attributed to an increasingly constrained local coordination environment at elevated salt contents, where ion–ion correlations and aggregate-like structures limit the ability of additional EC molecules to further modify cation–anion interactions. In this regime, ionic transport is governed predominantly by collective ion–ion effects rather than solvent-mediated screening. For the Na-based electrolytes, a small residual EC dependence persists at low EC fractions, likely reflecting the larger ionic radius and softer solvation environment of Na^+ ion.

When comparing Li- and Na-based electrolytes across different temperatures, qualitatively similar trends are observed. This behavior is illustrated and discussed in more detail in the SI (Section S10), where predictions for the individual Arrhenius parameters S_i are compared in detail (Section S11).

3.2 Generation of the Na-data set and evaluation of the AL procedure

Here, we analyze the data acquired by the active learning (AL) procedure and examine how the prediction error evolves with increasing generation number. The mean squared error (MSE) of the prediction for the ionic conductivity at $T = 20$ °C is shown in Fig. 4a. Two different strategies for selecting the test data are compared. In the first approach, test data are drawn from all generations, whereas in the second approach only data from Gen0 are used as the test set. The former strategy provides a representative assessment over the entire collected data set, while the latter has the advantage that the test data are fixed from the outset and are more uniformly distributed in feature space than data from Gen1 and Gen2. In both cases, the MSE is averaged over different test selections using leave-one-out cross-validation (LOO-CV).

For Gen0, both approaches necessarily yield the same MSE, amounting to 1.5×10^{-2}. For Gen1, the first approach results in an MSE of 4.7×10^{-3}, whereas the second approach yields a considerably smaller value of 2.2×10^{-3}. A similar trend is observed for Gen2, where the MSEs further decrease to 2.3×10^{-3} and 1.3×10^{-3}, respectively.

The higher error obtained with the first approach can be attributed to the fact that in particular Gen1 predominantly contains data points located near the boundaries of the feature space. When such boundary points are selected for testing, the models are evaluated in regions that are less densely covered by training data, which increases the local prediction uncertainty and leads to higher errors. In contrast, Gen0 data are mainly located near the center of the feature space, where the training data density is higher. Using these points for testing therefore predominantly probes interpolation within well-sampled regions, which typically results in lower errors.

The data collected in Gen2 are distributed more uniformly across the feature space than those in Gen1, indicating that the IDEAL acquisition function successfully improved the coverage of boundary regions during Gen1. Once these boundary regions were sufficiently populated, IDEAL preferentially sampled more central regions of the feature space in Gen2, thereby increasing the local data density and reducing interpolation errors. The corresponding distributions of the sampled data for each generation are shown in Fig. 4b and c.

3.3 Numerical AL simulations

Since it is infeasible to quantify the advantage of active learning (AL) over random sampling directly from the experimental data, additional numerical simulations with synthetic data were performed. These synthetic data mimic the experimental ground truth, including realistic levels of experimental noise. To this end, NN models were trained on the full experimental data set and subsequently used to generate synthetic values of the Arrhenius parameters S_i and the corresponding ionic conductivities across the entire feature space.

The discussion in the main text focuses on the models for S_0. Results for the models of S_1, S_2, and the ionic conductivity at $T = 20$ °C are provided in the SI (Section S12). The results of the numerical simulations for the S_0 model are shown in Fig. 5.

For comparison, six different data-acquisition strategies were considered in the simulations: (1) selection of 24 initial data points using the GSx approach, followed by IDEAL-based acquisition (blue line); (2) selection of a single random initial data point followed by IDEAL-based acquisition for all subsequent points (orange line); (3) selection of 24 initial data points using GSx, followed by random sampling (black line); (4) purely random sampling (gray line). In addition, (5) Latin Hypercube Sampling (LHS)[59] and (6) GSx sampling in batches of 24, 48, and 72 data points were included as reference strategies that do not rely on the underlying model.

(Fig. 5a) provides an overview of the averaged MSE as a function of the number of training data points N up to $N = 500$, which corresponds to the maximum number of data points considered. Standard errors are indicated by transparent shaded areas. Note that the results shown correspond to a batch size of one data point. However, the independence of the learning curves from the batch size was verified in the SI (Section S7).

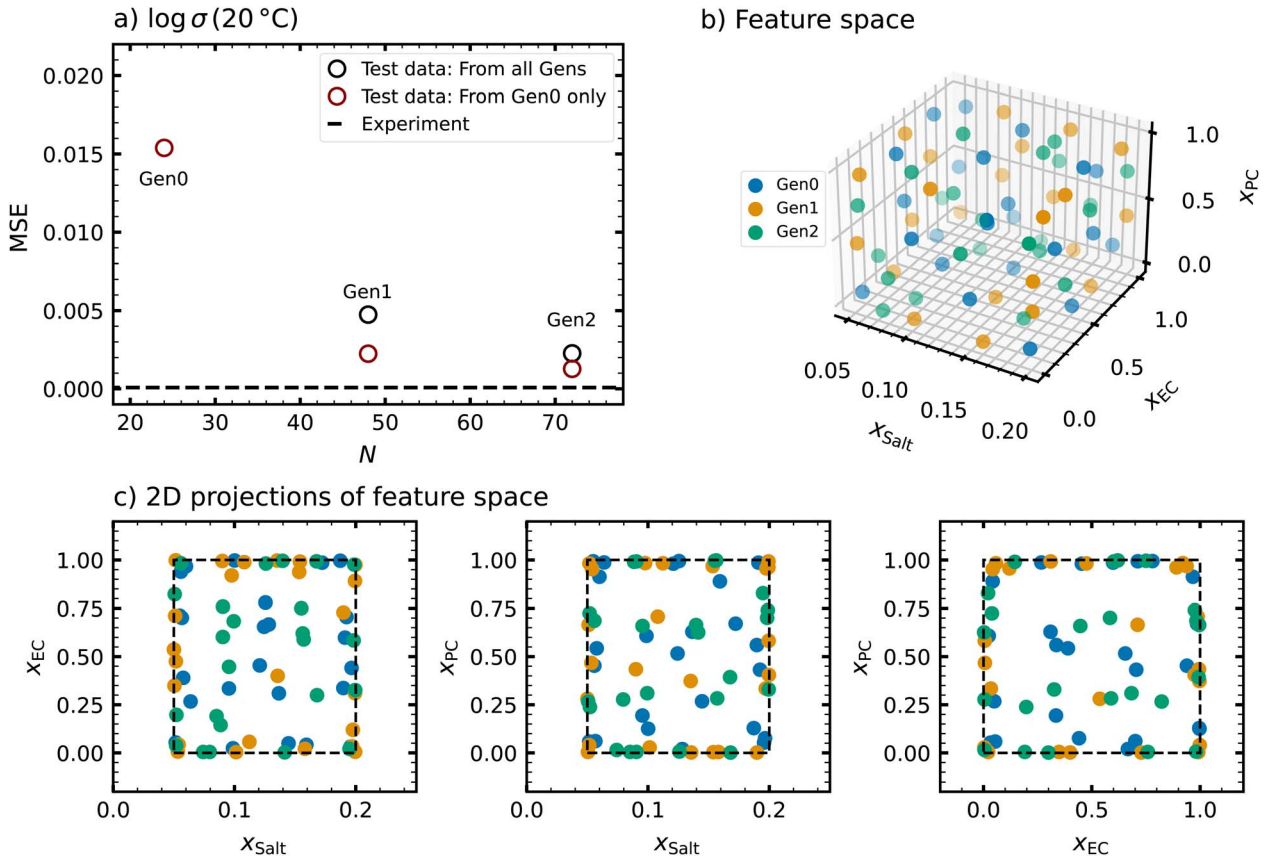

Fig. 4 (a) Dependence of the MSE for the prediction of the ionic conductivity of Na-based electrolytes on the number of training data N. The test data was selected using two different approaches. In the first approach data from all considered Gens was selected for testing, in the second approach only data from Gen0 was selected for testing. (b) Sampled data points within the feature space. Each generation of data was colored differently. (c) 2-Dimensional projections of the feature space and sampled data points. The black dashed rectangles indicate the boundaries for the acquisition of new data.

Purely random sampling exhibits the slowest reduction of the MSE with increasing N. Latin Hypercube Sampling (LHS) does not provide a systematic improvement over random sampling in this setting, indicating that uniform space-filling alone is not sufficient to efficiently reduce model errors in the present system. This behavior reflects the combination of a low-dimensional, physically constrained feature space and comparatively low experimental noise, for which additional data points are most informative when they expand the effective coverage of the response surface rather than merely densifying it. In contrast, GSx yields a substantially lower initial MSE by selecting maximally separated compositions that span the boundaries of the feature space. Even when subsequent data points are acquired by random sampling, the models initialized with GSx retain a clear advantage over purely random acquisition. This demonstrates that, in low-dimensional electrolyte composition spaces with smooth structure, early sampling of extreme compositions is particularly effective at reducing model bias and accelerating learning.

Strategies (1) and (2), which employ the IDEAL acquisition function, exhibit the fastest decrease of the averaged MSEs and clearly outperform the feature-based GSx approach. (Fig. 5b) focuses on the regime up to $N = 72$ and compares strategy (1), which combines an initial GSx batch with subsequent IDEAL acquisition, to strategy (2), which applies IDEAL from the outset. After the initial batch of 24 data points, strategy (2) yields a lower MSE (4.3×10^{-4}) than strategy (1) (7.4×10^{-4}), indicating a short-term advantage of direct IDEAL sampling. With increasing data set size, however, the two strategies rapidly converge. After acquisition of the second and third batches ($N = 48$ and $N = 72$), both approaches achieve very similar MSEs within the bounds of the standard errors, finally reaching values only about a factor of two above the experimental error (MSEs of 1.4×10^{-4} and 1.0×10^{-4} after Gen1 and Gen2, respectively). Further reductions would therefore require a disproportionate increase in the number of data points and are of limited practical relevance. For example, for $N = 96$ we report an MSE of 8×10^{-5}, clearly showing that the MSE decreases with a slower rate when adding further batches of data compared to the initial two batches. This convergence reflects the transition from a bias-dominated to a variance-limited learning regime: once the dominant structure of the low-dimensional and smooth response surface is captured, the remaining error is primarily governed by statistical variance and experimental noise rather than by the choice of the initial sampling strategy.

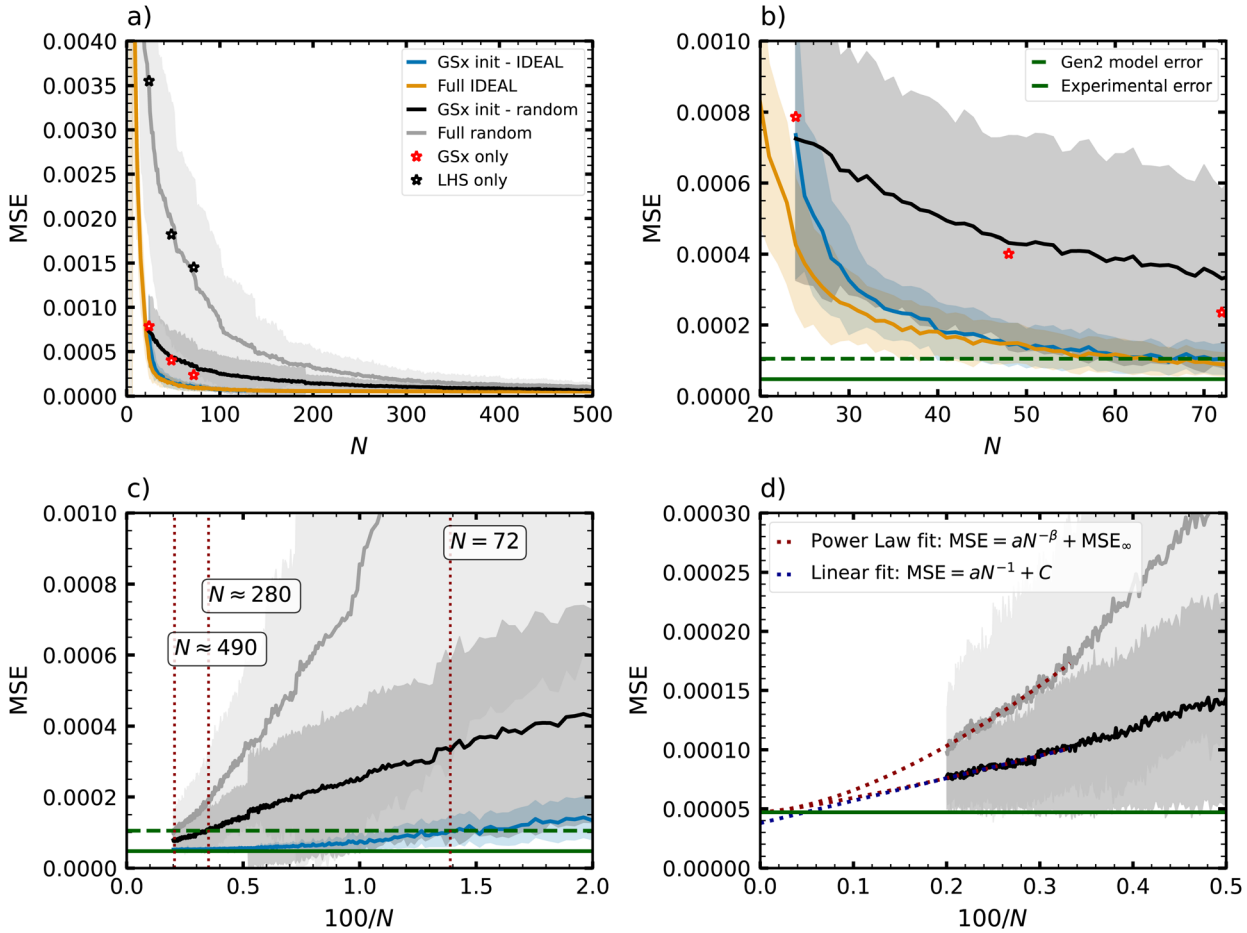

Fig. 5 Dependence of the MSE for the prediction of S_0 for Na-based electrolytes on (a) and (b) the number of training data N and (c) and d) $100/N$ in numerical simulations. Random data acquisition is compared to IDEAL-based data acquisition. The experimental error is shown as a black horizontal line and the error of a model trained on 72 data points is shown as a black dashed line. In (c) the vertical red lines indicate where different models hit that error. In (d) the power law fit in the inverse-N representation is shown as a red dotted line and the linear fit is shown as a blue dotted line.

(Fig. 5c) quantifies how many data points are required, on average, to reach the same target MSE of 10^{-4} achieved by the optimal AL strategy (strategy (1)) after $N = 72$ data points, when data are acquired either randomly after an initial GSx batch (strategy (3)) or by purely random sampling (strategy (4)). Since this target error is reached at different scales, the MSE is plotted as a function of $100/N$. For strategy (3), approximately 280 data points are required to reach the MSE whereas even more than 490 data points are needed for purely random sampling. This corresponds to a reduction in the required number of data points by a factor of approximately 4–7 for the S_0 models when using AL-guided acquisition compared to non-adaptive sampling. Note that this reduction is smaller for models of S_1 (factor 2) and S_2 (factor 3 and 4), which is related to the higher intrinsic noise of the underlying data.

(Fig. 5d) shows that, for sufficiently large data sets ($N \gtrsim 300$), the MSE follows a power-law behavior of the form

$$\mathrm{MSE} = aN^{-\beta} + C \tag{4}$$

where C corresponds to the asymptotic error MSE_∞ and reflects the inherent experimental noise.

Such scaling behavior of the MSE with increasing training set size is well known and has been observed empirically for a wide range of models and data sets.[60–62] In the asymptotic, variance-limited regime ($N \to \infty$), the decay exponent is bounded by $\beta \leq 1$. For linear regression models, $\beta = 1$ can be shown analytically, as previously demonstrated for electrolyte conductivity models.[31] Under suitable conditions, a similar asymptotic scaling has also been established for neural networks.[61]

When extrapolating the data for GSx followed by random acquisition (black curve) to $N \to \infty$ (corresponding to $100/N \to 0$) while fixing $\beta = 1$, the y-axis intercept is expected to coincide with the experimental error if the asymptotic regime has been reached and systematic model errors have become negligible. The fitted intercept is observed to lie slightly below the experimental error, indicating that this regime has not yet been fully attained. Consistently, allowing β to vary yields an effective exponent of $\beta \approx 1.2$ for $N > 300$.

For fully random acquisition (gray curve), the asymptotic regime is approached even more slowly, with a fitted exponent of $\beta \approx 1.6$. Exponents $\beta > 1$ are characteristic of pre-asymptotic learning regimes in which the MSE is still dominated by systematic deviations of the predictions from the ground truth. In such regimes, the error can decay faster than $1/N$, and adaptive data acquisition can accelerate this decay by reducing model bias. Once the variance-limited regime is reached, however, the MSE decreases at most as $1/N$, and the influence of the acquisition strategy becomes marginal.[36]

Using the NN model trained on the full Na-based electrolyte data set after Gen2, electrolyte formulations with the highest predicted ionic conductivity at various temperatures can be identified directly. To locate these maxima within the continuous feature space, a Particle Swarm Optimization (PSO) algorithm was employed.[63,64] PSO was chosen as a robust, gradient-free global optimization method that operates solely on the trained surrogate model and does not require additional experimental evaluations.

In principle, further refinement of the identified formulations could be achieved using, *e.g.*, Bayesian optimization. However, such methods typically require additional experiments that are performed sequentially and are therefore less compatible with parallel HTE. Moreover, the predicted conductivity landscapes exhibit broad plateaus of high ionic conductivity rather than sharp, isolated maxima. Under these conditions, further optimization would yield only marginal gains at disproportionately high experimental cost and is therefore not pursued here.

The optimized electrolyte formulations predicted by the NN and GPR models after Gen2, corresponding to the highest ionic conductivity at each temperature, are summarized in Table 1. The predictions clearly indicate that no single electrolyte formulation is optimal across the entire temperature range, in agreement with our previous findings for Li-based electrolytes.[22]

Instead, two systematic trends emerge with increasing temperature. First, the optimal salt fraction x_{Salt} increases from approximately 0.07 at −20 °C to about 0.10 at 60 °C, corresponding to an increase in salt concentration from 0.80 to 1.27 mol kg^{-1}. Second, the optimal EC content increases with temperature, while the PC content decreases. For the GPR model, the increase in EC concentration is slightly smaller and the decrease in PC concentration more pronounced compared to the NN predictions. Overall, both models predict very similar maximum ionic conductivities located at a broad plateau. Thus, small differences in the predictions of the ionic conductivity can lead to different optimal compositions, which are observed when comparing models. Whereas the $NaPF_6$ concentration is comparable and only differs by 0.1 mol kg^{-1} at 60 °C, x_{PC} and x_{EC} between the two model predictions differ quite substantially. As an example at −20 °C x_{PC} predicted by GPR is 0.31, while the NN model only predicts 0.17. For 20 °C the x_{PC} dependency for both model predictions becomes zero, while the increase of x_{EC} at 40 °C and 60 °C is predicted to be higher for the NN model with 0.86 and 0.99 compared to 0.78 and 0.79 for GPR.

The experimentally measured ionic conductivities show good agreement with the model predictions within the stated uncertainties. A systematic overprediction is observed at −20 °C for both models, which correlates slightly with increased model errors at temperatures far from the onset temperature used in the Arrhenius parametrization. Whereas the overprediction is within uncertainties for the NN predictions, it is much larger for the GPR predictions. It turned out that the GPR model predicted a second maximum at significantly higher EC concentrations when varying x_{EC} in the presence of PC while keeping the other features constant. It is known already from our previous publication that the GPR model with the anisotropic Matern kernel tends to produce non-physical fluctuations in the predictions.[22] In contrast the NN prediction is much smoother with only a single maximum as would be expected and which corresponds better to experimental results (see Section S9).

In addition, optimal electrolyte formulations were identified for the Li-based system using $LiPF_6$ as the conducting salt. Here, x_{EC} and x_{PC} were restricted to a maximum value of 0.75 due to the limited coverage of higher solvent fractions in the available Li-based data set. The corresponding NN predictions are summarized in Table S3. Compared to the Na-based system, the optimal $LiPF_6$ concentrations are consistently lower across all temperatures, ranging from 0.56 mol kg^{-1} at −20 °C to 0.89 mol

Table 1 Na-based electrolyte formulations with the highest predicted ionic conductivity at given temperatures. EC/PC and EC/EMC correspond to standard mixtures (see main text)

Model	T [°C]	x_{Salt}	x_{EC}	x_{PC}	$NaPF_6$ [mol kg^{-1}]	EC [w%]	PC [w%]	EMC [w%]	σ_{pred} [mS cm^{-1}]	σ_{exp} [mS cm^{-1}]
NN	−20	0.073	0.46	0.17	0.80	0.35	0.17	0.48	3.5 ± 1.1	2.8 ± 0.2
	0	0.077	0.51	0.17	0.86	0.38	0.18	0.44	6.4 ± 1.1	5.5 ± 0.1
	20	0.084	0.60	0.12	0.96	0.48	0.13	0.39	9.3 ± 1.1	9.0 ± 0.3
	40	0.087	0.86	0.00	1.05	0.84	0.00	0.16	14.0 ± 1.6	15.1 ± 0.6
	60	0.10	0.99	0.00	1.27	0.99	0.00	0.01	19.1 ± 2.4	19.5 ± 0.1
GPR	−20	0.071	0.72	0.31	0.80	0.45	0.34	0.21	3.8 ± 1.1	2.3 ± 0.2
	0	0.073	0.68	0.25	0.83	0.47	0.26	0.27	6.0 ± 0.8	5.4 ± 0.1
	20	0.083	0.63	0.05	0.96	0.56	0.06	0.38	9.4 ± 0.8	9.0 ± 0.3
	40	0.089	0.78	0.00	1.07	0.74	0.00	0.26	14.0 ± 0.9	14.7 ± 0.1
	60	0.097	0.79	0.00	1.17	0.76	0.00	0.24	19.4 ± 1.6	19.6 ± 0.1
EC/PC	20	0.086	1.00	0.46	1.00	0.50	0.50	0.00	7.6 ± 0.9	7.2 ± 0.4
EC/EMC	20	0.090	0.34	0.00	1.00	0.30	0.00	0.70	7.5 ± 1.0	7.8 ± 0.3

kg^{-1} at 60 °C. While the EC content of the optimized Li-based electrolyte is comparable to the Na-based case at low temperatures, it is lower at elevated temperatures. The PC fraction is also lower for the optimized Li-based electrolytes and shows only a weak temperature dependence.

The predicted maximum ionic conductivity of the optimized Li-based electrolytes is slightly lower than that of the corresponding Na-based electrolytes. This trend is consistent with literature reports for comparable $LiPF_6$- and $NaPF_6$-based electrolytes in EC : DEC (1 : 1 V/V) mixtures[65] and in pure PC.[66] At the same time, the relative conductivity of Li- and Na-based electrolytes is known to depend sensitively on the solvent composition, as $LiPF_6$ exhibits higher conductivity than $NaPF_6$ in pure DEC.[66] This highlights the need for systematic, composition-resolved investigations of non-aqueous electrolytes, as enabled by the AL-guided HTE approach employed in this work.

4 Impact of temperature-optimized Na-based electrolytes on galvanostatic cycling performance

To evaluate whether conductivity-driven electrolyte selection translates into improved electrochemical performance, temperature-optimized electrolyte formulations predicted by the NN and GPR models (Section 3.4) were selected for galvanostatic cycling performance evaluation in layered oxide||hard carbon sodium-ion coin cells. Electrolyte formulations optimized for maximum ionic conductivity at −20 °C, 20 °C, and 60 °C were selected and benchmarked against two literature-based reference electrolytes (1 mol kg^{-1} $NaPF_6$ in EC/PC and EC/EMC). All electrolyte compositions investigated in lab-cell experiments are listed in Table 1. Galvanostatic rate capability tests followed by prolonged cycling at moderate C-rate were used to probe performance across a broad range of operating conditions (Fig. 6).

In Fig. 6a–c the result of the rate-test is depicted. For all cells, a decrease of discharge capacity with increase of the C-rate was observed as expected. For the cells operated at −20 °C, an overall low initial discharge capacity was obtained, which is attributed to the low ion mobility at this temperature. Moreover, starting from 2C, for the cells containing reference electrolytes, no charge could be extracted from the cells using the reference electrolytes. At 5C, also the optimized electrolyte was no longer able to enable galvanostatic cycling of the cells, hinting at a limitation of the electrolyte for high C-rates. Throughout the rate-test at all three temperatures, the cells containing NN-optimized electrolyte showed an increased specific discharge capacity during the rate-test, which is most evident at low C-rates at low temperature and high C-rates at high temperature. At 20 °C, and at low C-rates, all cells showed similar discharge capacities. For the first cycle a low specific discharge capacity for the cells containing the NN-optimized of 112 mAh g^{-1} was obtained, which is the lowest of all cells. Yet the cells containing the NN-optimized electrolyte exhibited a slightly higher specific discharge capacity for the following cycles starting with 121 mAh g^{-1} for the second cycle, compared to 119 mAh g^{-1} for the reference counterpart. Beginning at 0.5C, for the cells containing the NN-optimized electrolyte the highest achievable specific discharge capacity and less fading compared to the cells containing EC/PC-, EC/EMC-based and GPR-optimized electrolyte is observed. At 60 °C, during the rate-test the cells containing NN-optimized electrolyte outperformed the cells containing the reference electrolytes and the cells containing GPR-optimized electrolyte. The same trend is evident, albeit less pronounced than at 20 °C. Interestingly, at 60 °C the C-rate performance was overall better than at 20 °C for all considered electrolyte formulations, resulting in similar discharge capacities at 1C and 20 °C as well as 2C and 60 °C. This is a strong indication of kinetic limitations within the electrode active materials and showcases the importance of electrolyte tuning even with the comparatively low maturity levels of the SIB technology. During the galvanostatic cycling at 0.5C for 100 cycles all three investigated temperatures, depicted in Fig. 6d–f, the cells containing NN-optimized electrolytes demonstrated better performance in comparison to the reference counterparts. The cells containing the GPR-optimized electrolyte showed inferior electrochemical performance, even lower than the reference counterparts at 20 °C. This difference can be contributed to the impact of the electrolyte components on the SEI. Whereas it is known that the presence of PC has an impact on the SEI formation on hard carbon, the specific effect depends on the exact electrolyte environment.[67–69] Thus, it is expected that although different concentrations of EC, PC and EMC may show a similar ionic conductivity, the SEI will be different and thus also the electrochemical performance of the resulting cells. At 60 °C the cells containing the NN-optimized electrolyte showed the highest initial specific discharge capacity, but a higher fading, leading to an overlap of the discharge capacities after 50 cycles and slightly higher discharge capacity for the cells containing the GPR-optimized electrolyte after 100 cycles. At −20 °C, an extremely low capacity for the two reference counterparts and the GPR-optimized electrolyte was achieved, with the cells containing the NN-optimized electrolyte tripling the achievable specific discharge capacity of 30 mAh g^{-1}. However, it is immediately evident that at −20 and 20 °C none of the cells recovered the specific capacities previously achieved at 0.5C during the rate-test, indicating that the preceding high-rate steps induce irreversible changes and that electrode kinetics and degradation processes impose limitations that cannot be overcome by electrolyte optimization alone. At 60 °C, capacity recovery at 0.5C is more complete for most formulations, consistent with reduced kinetic limitations at elevated temperature. It must be stressed here again that the models are completely agnostic to galvanostatic cycling performance and only optimized for ionic conductivity. The difference in electrochemical performance between the NN and GPR-optimized electrolyte, visible in both the rate capability and subsequent data at 0.5C, reflects the broad plateau of high ionic conductivity identified in composition space and therefore is consistent with the models own confidence intervals. It demonstrates that although ionic conductivity is a useful guiding metric but it does not uniquely determine cell

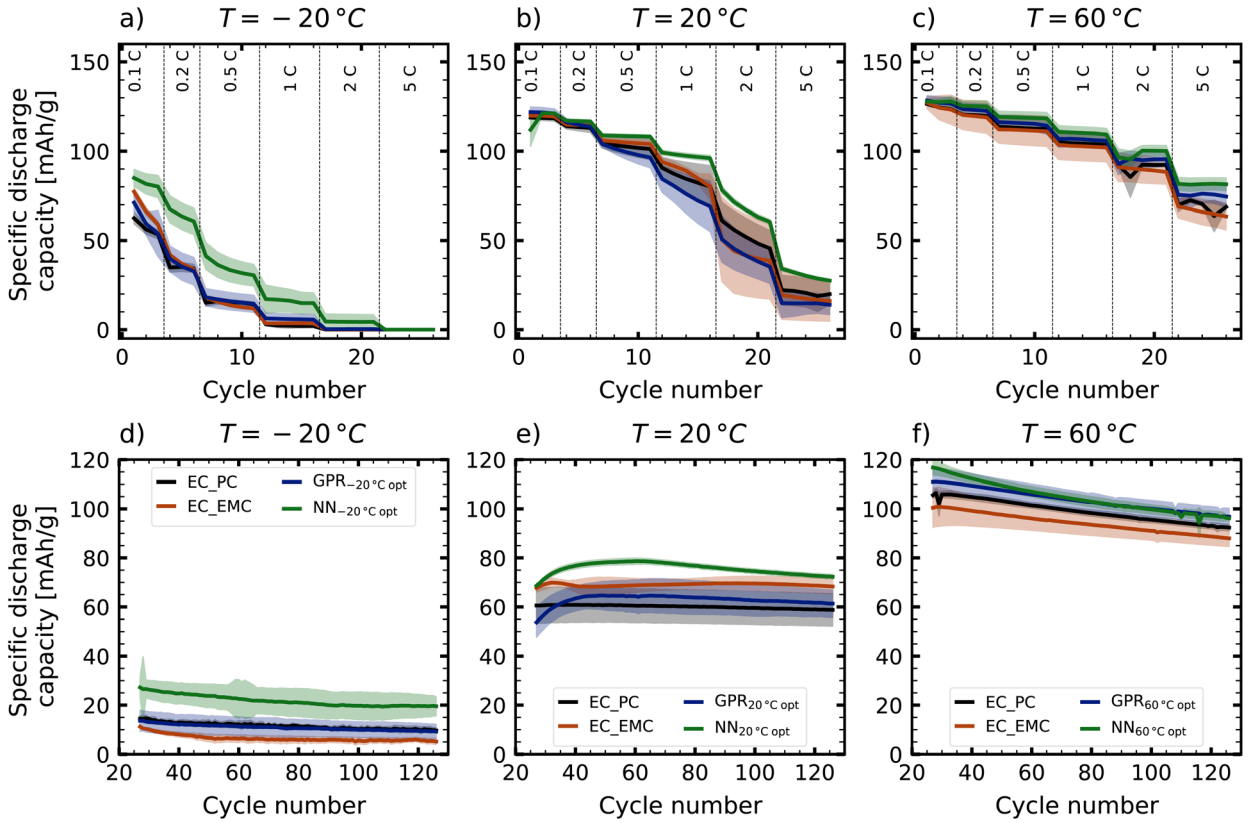

Fig. 6 Specific discharge capacities *vs.* cycle number of layered oxide||hard carbon coin cells with electrolyte formulations optimized by NN and GPR models compared to literature derived electrolyte formulations EC/EMC and EC/PC. Results of rate tests comprised of 3 × 0.1C, 3 × 0.2C, 5 × 0.5C, 5 × 1C, 5 × 2C, 5 × 5C at (a) −20 °C, (b) 20 °C and (c) 60 °C. Charge/discharge cycling with 0.5C for the same cells for 100 cycles at (d) −20 °C, (e) 20 °C and (f) 60 °C.

performance. Nevertheless, these small differences between the two models allow us to gain additional insights into the correlation of electrolyte composition and galvanostatic cycling performance.

5 Conclusion

In this study, we presented a workflow that couples HTE with AL to systematically map and model non-aqueous lithium- and sodium-based electrolyte formulations. In contrast to conventional approaches that primarily aim at identifying a single optimal composition *via* Bayesian optimization, the presented strategy focuses on constructing predictive surrogate models over the full space of physically reasonable electrolyte formulations. This enables a comprehensive understanding of how electrolyte composition and temperature jointly govern ionic conductivity. The batch-wise AL approach is inherently compatible with parallel experimentation, thereby avoiding time-consuming serial optimization loops. Owing to its modular design, the workflow can be readily extended to other electrolyte systems and experimental objectives.

Training NN surrogate models on both data sets enabled a direct, composition-wide comparison of $LiPF_6$- and $NaPF_6$-based electrolytes within an identical feature representation for EC-, EMC-, and PC-containing solvent mixtures. This analysis indicates that Na-based electrolytes tend to exhibit slightly higher ionic conductivities than their Li-based counterparts at comparable compositions, particularly at low salt and EC contents as well as at elevated salt concentrations. At the same time, the overall regions of high ionic conductivity in composition space are very similar for both cations, and the observed differences remain modest across the investigated temperature range. The pronounced sensitivity of ionic conductivity to the EC content is consistent with previous reports linking EC-rich environments to reduced cation–anion association and enhanced charge carrier mobility. The persistence of this trend in both electrolyte systems suggests that EC primarily modulates the local solvation environment rather than inducing strongly cation-specific effects, with a more pronounced influence in lithium-based electrolytes.

Within this framework, a new data set for Na-based electrolytes was generated using an initial GSx sampling followed by IDEAL-based refinement. Numerical AL simulations on synthetic data demonstrate that prioritizing informative compositions, particularly near the boundaries of composition space, substantially accelerates model convergence. The considered formulation space can be reliably described using only 72 unique electrolyte compositions acquired over two AL iterations, corresponding to a reduction in required data points by a target-dependent factor, which is approximately 4–7 for S_0,

compared to random sampling strategies. These results highlight the efficiency gains enabled by combining HTE with AL.

Galvanostatic cycling experiments further indicate that enhanced ionic conductivity can serve as a useful guiding parameter for improving cell performance in non-aqueous aprotic electrolytes, particularly under kinetically demanding conditions. Even at extreme operating conditions such as −20 °C, noticeable performance improvements are achieved solely by adjusting the formulation of otherwise identical electrolyte components. At the same time, the results demonstrate that ionic conductivity alone is not sufficient to universally predict full-cell performance, reflecting the complex interplay of transport properties, interfacial processes, and electrode kinetics during galvanostatic cycling.

In this context, the value of the present approach lies not in identifying a single optimal formulation, but in constructing a comprehensive, composition-wide surrogate model that disentangles the relative importance of electrolyte components across temperatures and operating regimes. By combining HTE with AL and physically informed feature representations, the workflow enables efficient and interpretable exploration of chemically constrained formulation spaces. This holistic framework moves electrolyte research beyond trial-and-error optimization toward systematic understanding and provides a general and transferable basis for rational electrolyte discovery and multi-criteria design across a wide range of battery chemistries and performance metrics.

6 Experimental

6.1 Electrolyte formulation

Sodium hexafluorophosphate ($NaPF_6$), ethylene carbonate (EC), ethyl methyl carbonate (EMC) and propylene carbonate (PC) for the Na-based electrolytes were all purchased from E-lyte Innovations GmbH in battery grade quality and used without further purification. All considered electrolytes were formulated in the glovebox with $NaPF_6$ as the conducting salt, a blend of EC, PC and EMC as electrolyte solvents. The $NaPF_6$ concentration was allowed to vary between 0.5 and 2.7 mol kg^{-1}. In total, 72 electrolytes were formulated.

6.2 Ionic conductivity determination

An inert gas environment was rigorously maintained during all experiments using a nitrogen filled glovebox (GS Glovebox, maintaining H_2O and O_2 values < 1 ppm). The ionic conductivity of the electrolyte formulations was determined according to Krishnamoorthy *et al.*[31] The cell constants were determined using a conductivity standard (0.01 M KCl in H_2O, 1.276 mS cm^{-1}) averaged over at least 5 measurements. As sample containers 2 mL Eppendorf Safe-Lock tubes were used and each filled with 750 μL of electrolyte. The impedance measurements were carried out using our in-house designed electrodes.[70] A frequency range between 20 kHz and 50 Hz was applied on a Metrohm Autolab/M204 potentiostat/galvanostat with 12 channels and 8-channel multiplexer, summing up to 96 channels. The samples were equilibrated for 2 h inside a Memmert TTC256 climatic chamber with 0.1 °C temperature accuracy prior to every measurement. Measurements were carried out in the temperature range of −20 °C and 60 °C with increments of 10 °C. Using the Metrohm Nova software, the obtained impedance spectra were fitted with a predefined equivalent circuit (R_s(CPE-R_p)) after each measuring point.

6.3 Materials and cell assembly

Positive and negative electrodes from commercially available 220 mAh (16 g cm^{-2}) layered oxide||hard carbon dry pouch cells (Li-FUN Technology) were harvested. The double-sided coating was removed on one side using water. From the sheets, discs with 15 mm for the anode and 14 mm for the cathode were punched out and dried for 12 h at 120 °C under reduced pressure. Whatman GF/D separator (Sigma-Aldrich) was punched into 17 mm discs and dried for 12 h at 90 °C under reduced pressure. All materials were stored inside the nitrogen filled glovebox prior to assembly. For the galvanostatic cycling performance evaluation, two electrode CR2032 type coin cells were assembled with one layer of Whatman GF/D as a separator between the 15 mm hard carbon anode and the 14 mm layered oxide cathode with a fixed volume of electrolyte of 60 μL.

6.4 Galvanostatic cycling protocol

For galvanostatic cycling a voltage range of 2.0 to 4.0 V was applied using a Maccor Series 4000 battery tester. Prior to any galvanostatic cycling a rest step at OCV for 6 h was performed. For the galvanostatic cycling performance evaluation, a rate test comprised of 3 × 0.1C, 3 × 0.2C, 5 × 0.5C, 5 × 1C, 5 × 2C, 5 × 5C, was followed by galvanostatic cycling for 100 cycles at 0.5C. To validate reproducibility, three coin cells per electrolyte formulation were assembled and all measurements were conducted at the respective target temperatures of −20 °C, 20 °C, and 60 °C.

6.5 Active learning iterations

For the AL iterations the feature x_{Salt} was limited to the interval (0.05, 0.20) as the interesting range of conducting salt concentrations. The other features were not limited. For the model training and acquisition function calculation the feature was scaled to the interval (0, 1) using scikit-learns MinMax-scaler,[38] such that in the modelling process all features were selected from the same interval. All features were treated equally for the calculation of the IDEAL acquisition function and applied to identify the suggested data point for Gen1 and Gen2. The maximum of the acquisition function was determined with particle swarm optimization with $c_1 = 0.5$, $c_2 = 0.3$ and $w = 0.9$.[71] For Gen0, 50 agents were used for 50 iterations. For Gen1 and Gen2 the same number of agents were used for 200 iterations. For further details see the SI Section S2 and S3.

6.6 Calculation of the mean squared error

The MSE for the prediction of the logarithmic ionic conductivity at $T = 20$ °C was evaluated using two different cross-validation

approaches. In the first approach, leave-one-out cross-validation (LOO-CV) was performed using all available data after completion of Gen0, Gen1 and Gen2, representing the full state of knowledge. Since one data point is used for testing, the MSEs are calculated for the remaining 23, 47 and 71 data points. In the second approach, the models were trained on similar data as in the first approach, but used only data from Gen0 for testing. Each data point from Gen0 was used once for testing, as in the LOO-CV approach. This is motivated by the fact that the acquisition function does not choose equally distributed data points in the feature space (see Fig. 4) and thus the MSE might be biased because some regions might be under- and others might be over-represented. Ideally, one would use completely equally distributed data points for testing to obtain a reliable model error, however, this is not possible in the experimental setup. As a compromise data from Gen0 was used for testing, which turned out to be most equally distributed from all generations (Gen0, Gen1 and Gen2). Furthermore, this data was known from the beginning so that it could be used in all subsequent generations for testing.

6.7 Details on numerical active learning simulations

From the experimental data, it is infeasible to estimate the advantage of AL over random sampling directly, since the pool was created by AL. To estimate the reduction of electrolyte formulations needed to fit an accurate model, numerical AL simulations were performed. For these simulations, models for the S_i, trained on all experimental data of the Na-data set, were defined as ground truth. Whenever new data needed to be labeled with the ionic conductivity, the ground truth models were evaluated instead of performing experiments in the laboratory. For each prediction of the ground truth models, Gaussian noise was added with a variance that mimics the experimental variance of the S_i. In principle, this is the only source of errors. Since the ground truth and the regression model are similar in architecture, no model error is expected for a sufficiently large number of data and well-optimized parameters. The test error is calculated for test data points on a fixed grid of 10 data points per dimension, summing up to 1000 data points, which cover the feature space equally well and ensure that the obtained error is representative for the full feature space. This setup allows a rapid evaluation and screening of different choices of initial data and a comparison of different data acquisition approaches.

Author contributions

M. Fischer: conceptualization, data curation, formal analysis, methodology, software, validation, visualization, writing – original draft. R. T. Hinz: conceptualization, data curation, investigation, methodology, validation, visualization, writing – original draft. C. Wölke: methodology, supervision, writing – review. I. Cekic-Laskovic: project administration, supervision, writing – review & editing. M. Winter: funding acquisition, resources. A. Heuer: project administration, supervision, writing – review & editing.

Conflicts of interest

There are no conflicts to declare.

Data availability

Experimental data for the lithium and sodium-based data sets as well as relevant synthetic data corresponding to both data sets are available *via* Zenodo at https://doi.org/10.5281/zenodo.18429013. The scripts and jupyter-notebooks for data analysis and creation of Fig. 3–6 and most figures in the SI are available *via* Github and Zenodo at https://doi.org/10.5281/zenodo.20748573.

The python code of the LECA package is available *via* Github and Zenodo at https://doi.org/10.5281/zenodo.20703019. The implementation of the Active Learning library (PyALAF) is available *via* Github and Zenodo at https://doi.org/10.5281/zenodo.20747294.

Ref. 72–77 are cited in the supplementary information (SI). Supplementary information: a description and comparison of different acquisition functions, a description of the PyALAF package, a description of the data sets, example Arrhenius fits and a comparison of different ML models. Furthermore, model predictions for sodium and lithium are evaluated and compared in detail. Information about optimized lithium electrolytes is provided. Additional information for numerical active learning simulations and scanning electron microscopy and energy-dispersive X-ray spectroscopy images of the electrode. See DOI: https://doi.org/10.1039/d6dd00149a.

Acknowledgements

The authors thank D. Diddens and P. Yan for fruitful discussions and helpful insights in lithium- and sodium-based electrolytes. M. F. acknowledges funding from the BMBF (InterKI, 16DHBKI049). R. T. H. acknowledges funding from the European Union's Horizon 2020 research and innovation programme under grant agreement No. 958174 (SuSaNa). This work was supported by the Helmholtz Association within the framework of the Helmholtz-Innopool project AutoMat.

Notes and references

1 N. Tapia-Ruiz, A. R. Armstrong, H. Alptekin, M. A. Amores, H. Au, J. Barker, R. Boston, W. R. Brant, J. M. Brittain, Y. Chen, M. Chhowalla, Y.-S. Choi, S. I. R. Costa, M. Crespo Ribadeneyra, S. A. Cussen, E. J. Cussen, W. I. F. David, A. V. Desai, S. A. M. Dickson, E. I. Eweka, J. D. Forero-Saboya, C. P. Grey, J. M. Griffin, P. Gross, X. Hua, J. T. S. Irvine, P. Johansson, M. O. Jones, M. Karlsmo, E. Kendrick, E. Kim, O. V. Kolosov, Z. Li, S. F. L. Mertens, R. Mogensen, L. Monconduit, R. E. Morris, A. J. Naylor, S. Nikman, C. A. O'Keefe, D. M. C. Ould, R. G. Palgrave, P. Poizot, A. Ponrouch, S. Renault, E. M. Reynolds, A. Rudola, R. Sayers, D. O. Scanlon, S. Sen, V. R. Seymour, B. Silván, M. T. Sougrati, L. Stievano, G. S. Stone, C. I. Thomas,

M.-M. Titirici, J. Tong, T. J. Wood, D. S. Wright and R. Younesi, *J. Phys.: Energy*, 2021, **3**, 031503.
2 E. Goikolea, V. Palomares, S. Wang, I. R. de Larramendi, X. Guo, G. Wang and T. Rojo, *Adv. Energy Mater.*, 2020, **10**, 2002055.
3 C. Delmas, *Adv. Energy Mater.*, 2018, **8**, 1703137.
4 H. Li, F. Wu, J. Wang, J. Wang, H. Qu, M. Chen, H. Zhang and S. Passerini, *Energy Environ. Sci.*, 2025, **18**, 3887–3916.
5 S. Y. Hong, Y. Kim, Y. Park, A. Choi, N.-S. Choi and K. T. Lee, *Energy Environ. Sci.*, 2013, **6**, 2067–2081.
6 X. Zheng, L. Huang, X. Ye, J. Zhang, F. Min, W. Luo and Y. Huang, *Chem*, 2021, **7**, 2312–2346.
7 Z. Hu, L. Liu, X. Wang, Q. Zheng, C. Han and W. Li, *Adv. Funct. Mater.*, 2024, **34**, 2313823.
8 N. Aslfattahi, L. Samylingam, M. S. Kiai, K. Kadirgama, V. Kulish, M. Schmirler and Z. Said, *J. Energy Storage*, 2023, **72**, 108781.
9 B. Qi, X. Zhang, L. You, X. Yu, Z. Qiao and D. Ruan, *J. Energy Storage*, 2024, **100**, 113523.
10 A. V. Sadybekov and V. Katritch, *Nature*, 2023, **616**, 673–685.
11 E. Gawehn, J. A. Hiss and G. Schneider, *Mol. Inf.*, 2016, **35**, 3–14.
12 J. R. Kitchin, *Nat. Catal.*, 2018, **1**, 230–232.
13 T. Toyao, Z. Maeno, S. Takakusagi, T. Kamachi, I. Takigawa and K.-I. Shimizu, *ACS Catal.*, 2020, **10**, 2260–2297.
14 H. Li, Y. Jiao, K. Davey and S.-Z. Qiao, *Angew. Chem. Int. Ed.*, 2023, **62**, e202216383.
15 R. E. A. Goodall and A. A. Lee, *Nat. Commun.*, 2020, **11**, 6280.
16 D. Jha, L. Ward, A. Paul, W.-K. Liao, A. Choudhary, C. Wolverton and A. Agrawal, *Sci. Rep.*, 2018, **8**, 17593.
17 A. Benayad, D. Diddens, A. Heuer, A. N. Krishnamoorthy, M. Maiti, F. L. Cras, M. Legallais, F. Rahmanian, Y. Shin, H. Stein, M. Winter, C. Wölke, P. Yan and I. Cekic-Laskovic, *Adv. Energy Mater.*, 2022, **12**, 2102678.
18 Y. Chen, Y. Liu, Z. He, L. Xu, P. Yu, Q. Sun, W. Li, Y. Jie, R. Cao, T. Cheng and S. Jiao, *Natl. Sci. Open*, 2023, 20230039.
19 M.-F. Ng, Y. Sun and Z. W. Seh, *Energy Adv.*, 2023, **2**, 449–464.
20 A. Valizadeh and M. H. Amirhosseini, *SN Comput. Sci.*, 2024, **5**, 717.
21 Y. Wang, *npj Comput. Mater.*, 2025, **11**, 89.
22 P. Yan, M. Fischer, H. Martin, C. Wölke, A. N. Krishnamoorthy, I. Cekic-Laskovic, D. Diddens, M. Winter and A. Heuer, *J. Mater. Chem. A*, 2024, **12**, 19123–19136.
23 D.-Z. Lin, K.-J. Pan, Y. Li, C. B., L. Zhang, K. N. Jayarapu, T. Li, J. V. Tran, W. A. Goddard, Z. Luo and Y. Liu, *Sci. Adv.*, 2025, **11**, eadu4391.
24 A. Dave, J. Mitchell, S. Burke, H. Lin, J. Whitacre and V. Viswanathan, *Nat. Commun.*, 2022, **13**, 5454.
25 S. Zhu, B. Ramsundar, E. Annevelink, H. Lin, A. Dave, P.-W. Guan, K. Gering and V. Viswanathan, *Nat. Commun.*, 2024, **15**, 8649.
26 A. Dave, J. Mitchell, K. Kandasamy, H. Wang, S. Burke, B. Paria, B. Póczos, J. Whitacre and V. Viswanathan, *Cell Rep. Phys. Sci.*, 2020, **1**, 100264.
27 F. Rahmanian, M. Vogler, C. Wölke, P. Yan, M. Winter, I. Cekic-Laskovic and H. S. Stein, *Batter. Supercaps*, 2022, **5**, e202200228.
28 J. Ruža, M. A. Stolberg, S. Cawthern, J. A. Johnson, Y. Shao-Horn and R. Gómez-Bombarelli, *Chem. Mater.*, 2025, **37**, 7771–7777.
29 J. Noh, H. A. Doan, H. Job, L. A. Robertson, L. Zhang, R. S. Assary, K. Mueller, V. Murugesan and Y. Liang, *Nat. Commun.*, 2024, **15**, 2757.
30 J. T. Yik, C. Hvarfner, J. Sjölund, E. J. Berg and L. Zhang, *Cell Rep. Phys. Sci.*, 2025, **6**, 102548.
31 A. Narayanan Krishnamoorthy, C. Wölke, D. Diddens, M. Maiti, Y. Mabrouk, P. Yan, M. Grünebaum, M. Winter, A. Heuer and I. Cekic-Laskovic, *Chem. Methods*, 2022, **2**, e202200008.
32 L. McInnes, J. Healy and S. Astels, *J. Open Source Softw.*, 2017, **2**, 205.
33 M. S. Ding, K. Xu, S. S. Zhang, K. Amine, G. L. Henriksen and T. R. Jow, *J. Electrochem. Soc.*, 2001, **148**, A1196.
34 J. Landesfeind and H. A. Gasteiger, *J. Electrochem. Soc.*, 2019, **166**, A3079.
35 B. Efron, *Ann. Stat.*, 1979, **7**, 1–26.
36 T. Hastie, R. Tibshirani and J. Friedman, *The Elements of Statistical Learning*, Springer, New York, NY, 2009.
37 M. Kirk, *Thoughtful Machine Learning: A Test-Driven Approach*, O'Reilly Media, Inc., 2014.
38 F. Pedregosa, G. Varoquaux, A. Gramfort, V. Michel, B. Thirion, O. Grisel, M. Blondel, P. Prettenhofer, R. Weiss, V. Dubourg, J. Vanderplas, A. Passos, D. Cournapeau, M. Brucher, M. Perrot and É. Duchesnay, *J. Mach. Learn. Res.*, 2011, **12**, 2825–2830.
39 D. C. Liu and J. Nocedal, *Math. Program.*, 1989, **45**, 503–528.
40 C. E. Rasmussen and C. K. I. Williams, *Gaussian Processes for Machine Learning*, The MIT Press, 2005.
41 E. Schulz, M. Speekenbrink and A. Krause, *J. Math. Psychol.*, 2018, **85**, 1–16.
42 B. Settles, *Active Learning Literature Survey*, 2009.
43 P. Kumar and A. Gupta, *J. Comput. Sci. Technol.*, 2020, **35**, 913–945.
44 P. Ren, Y. Xiao, X. Chang, P.-Y. Huang, Z. Li, B. B. Gupta, X. Chen and X. Wang, *ACM Comput. Surv.*, 2021, **54**, 1–40.
45 C. C. Aggarwal, X. Kong, Q. Gu, J. Han and P. S. Yu, in *Data Classification*, Chapman and Hall/CRC, 2014.
46 A. Bemporad, *Inf. Sci.*, 2023, **626**, 275–292.
47 F. Zhdanov, *arXiv*, 2019, preprint arXiv:1901.05954, DOI: 10.48550/arXiv.1901.05954.
48 T. N. C. Cardoso, R. M. Silva, S. Canuto, M. M. Moro and M. A. Gonçalves, *Inf. Sci.*, 2017, **379**, 313–337.
49 M. Balandat, B. Karrer, D. Jiang, S. Daulton, B. Letham, A. G. Wilson and E. Bakshy, *Adv. Neural Inf. Process. Syst.*, 2020, 21524–21538.
50 F. Di Fiore, M. Nardelli and L. Mainini, *Arch. Comput. Methods Eng.*, 2024, **31**, 2985–3013.
51 L. Breiman, *Mach. Learn.*, 2001, **45**, 5–32.
52 T. H. Cormen, C. E. Leiserson, R. L. Rivest and C. Stein, *Introduction to Algorithms*, MIT Press, Cambridge, MA, USA, 4th edn, 2022.

53 H. Yu and S. Kim, *IEEE International Conference on Data Mining*, 2010, pp. 1151–1156.
54 D. Wu, C.-T. Lin and J. Huang, *Inf. Sci.*, 2019, **474**, 90–105.
55 S. Seo, M. Wallat, T. Graepel and K. Obermayer, *Proceedings of the IEEE-INNS-ENNS International Joint Conference on Neural Networks. IJCNN 2000. Neural Computing: New Challenges and Perspectives for the New Millennium*, 2000, vol. 3, pp. 241–246.
56 C. Hvarfner, D. Eriksson, E. Bakshy and M. Balandat, *Informed Initialization for Bayesian Optimization and Active Learning*, 2025.
57 M. Maiti, A. N. Krishnamoorthy, Y. Mabrouk, N. Mozhzhukhina, A. Matic, D. Diddens and A. Heuer, *Phys. Chem. Chem. Phys.*, 2023, **25**, 20350–20364.
58 P. Zavalij, Y. Shoufeng and M. Wittingham, CCDC 244695: Experimental Crystal Structure Determination, 2005.
59 M. D. McKay, R. J. Beckman and W. J. Conover, *Technometrics*, 1979, **21**, 239–245.
60 D. Cohn, L. Atlas and R. Ladner, *Mach. Learn.*, 1994, **15**, 201–221.
61 Y. Bahri, E. Dyer, J. Kaplan, J. Lee and U. Sharma, *Proc. Natl. Acad. Sci.*, 2024, **121**, e2311878121.
62 T. Cadez and K.-M. Kim, *arXiv*, 2025, preprint arXiv:2509.10000, DOI: 10.48550/arXiv.2509.10000.
63 Y. Shi and R. Eberhart, *1998 IEEE International Conference on Evolutionary Computation Proceedings. IEEE World Congress on Computational Intelligence (Cat. No.98TH8360)*, 1998, pp. 69–73.
64 J. Kennedy and R. Eberhart, *Proceedings of ICNN'95 – International Conference on Neural Networks*, 1995, Vol. 4, pp. 1942–1948.
65 J. Landesfeind, T. Hosaka, M. Graf, K. Kubota, S. Komaba and H. A. Gasteiger, *J. Electrochem. Soc.*, 2021, **168**, 040538.
66 A. V. Cresce, S. M. Russell, O. Borodin, J. A. Allen, M. A. Schroeder, M. Dai, J. Peng, M. P. Gobet, S. G. Greenbaum, R. E. Rogers and K. Xu, *Phys. Chem. Chem. Phys.*, 2016, **19**, 574–586.
67 S. Y. Luchkin and E. M. Pazhetnov, *J. Mater. Chem. A*, 2024, **12**, 29795–29801.
68 C. Ryu, S.-B. Rim, Y. Kang and C.-J. Yu, *RSC Adv.*, 2023, **13**, 5627–5633.
69 J.-S. Kim, M.-J. Won, W. Pak, K.-H. Pak, C. Ryu and C.-J. Yu, *RSC Adv.*, 2026, **16**, 5427–5436.
70 H.-D. Wiemhöfer, M. Grünebaum and M. M. Hiller, *Utility Pat.*, WO2014139494, 2014.
71 L. J. Miranda, *J. Open Source Softw.*, 2018, **3**, 433.
72 T. Danka and P. Horvath, *arXiv*, 2018, preprint arXiv:1805.00979, DOI: 10.48550/arXiv.1805.00979.
73 D. Kottke, M. Herde, T. P. Minh, A. Benz, P. Mergard, A. Roghman, C. Sandrock and B. Sick, scikit-activeml: A Library and Toolbox for Active Learning Algorithms, 2021, preprints, DOI: 10.20944/preprints202103.0194.v1.
74 Y.-P. Tang, G.-X. Li and S.-J. Huang, *arXiv*, 2019, preprint arXiv:1901.03802, DOI: 10.48550/arXiv.1901.03802.
75 E. Surzhikova and J. Proppe, *Mach. Learn.: Sci. Technol.*, 2025, **6**, 025064.
76 T. Cordier, V. Blot, L. Lacombe, T. Morzadec, A. Capitaine and N. Brunel, *Proceedings of the Twelfth Symposium on Conformal and Probabilistic Prediction with Applications*, 2023, pp. 549–581.
77 K. He, X. Zhang, S. Ren and J. Sun, *arXiv*, 2015, preprint, arXiv:1502.01852, DOI: 10.48550/arXiv.1502.01852.